Engineering Fracture Mechanics 210 (2019) 203–211

Contents lists available at ScienceDirect

Engineering Fracture Mechanics

journal homepage: www.elsevier.com/locate/engfracmech

Damage monitoring of three-point bending concrete specimens by acoustic emission and resonant frequency analysis

Giuseppe Lacidogna, Gianfranco Piana*, Alberto Carpinteri

Department of Structural, Geotechnical and Building Engineering, Politecnico di Torino, Corso Duca degli Abruzzi 24, 10129 Torino, Italy

ARTICLE INFO

Keywords:
Acoustic emission
Resonant frequency
Crack growth
Finite element analysis
Concrete

ABSTRACT

The crack propagation process in pre-notched concrete beam specimens, tested in the lab under three-point bending, was monitored by the Acoustic Emission (AE) technique and the extraction of resonant frequencies. The loading process was carried out in displacement-controlled conditions up to the final failure of the specimen. Average frequency vs. RA value analysis was used to characterize the crack propagation mode, whereas the cumulative AE energy and the variation in the resonant bending frequencies were selected as the main parameters to monitor the damage progress due to crack advancement. Moreover, finite element models were implemented to reproduce the load–deflection curve and to evaluate the resonant frequencies for different notch depths. An inverse procedure was therefore applied to estimate the crack advancement based on the measured and calculated frequencies.

1. Introduction

The Acoustic Emission (AE) technique is a noninvasive, nondestructive monitoring method for investigating the damage evolution and predicting the remaining lifetime of laboratory samples and full-scale structures [1]. The AE signal analysis allows to obtain information about the cracking pattern, the prevailing fracture mode, and the achievement of critical conditions leading to collapse [2–8]. Furthermore, correlations between AE energy and damage evolution can also be carried out [9–10]. At the same time, nondestructive dynamic testing of structures allows to obtain information about stability [11–14] and/or damage level and location [15–25]. Indeed, it is known that variations in structural stiffness are revealed by variations in modal parameters (primarily, frequencies and curvatures). In this case, Dynamic Identification (DI) techniques are currently used to extract modal parameters starting from time measures of displacements (or strains), velocities or accelerations [26].

In a previous paper [27], the authors reported on laboratory monitoring of damage progress in pre-notched concrete specimens tested in four-point bending by the AE and DI techniques. In that paper, a correlation between the two sets of data is presented, and a general procedure for the structural health monitoring of complex structures by combining the two abovementioned nondestructive techniques is also outlined. Main advantages of such a mixed approach, especially in monitoring full-scale structures, are: (i) damage precursor/alert data provided by the AE technique; (ii) damage location based on measured AE and/or modal data; and (iii) direct information about the global structural stiffness, that can be correlated by numerical models tuned on measured modal characteristics to damage level and resisting capacity.

The present paper deals with specimens analogous to those analyzed in [27], although here they are tested in three-point bending and monitored by the same combined approach. In fact, it has been shown that concrete and mortar specimens tested in four-point

* Corresponding author.
E-mail address: gianfranco.piana@polito.it (G. Piana).

https://doi.org/10.1016/j.engfracmech.2018.06.034
Received 20 March 2018; Received in revised form 25 June 2018; Accepted 25 June 2018
Available online 26 June 2018
0013-7944/

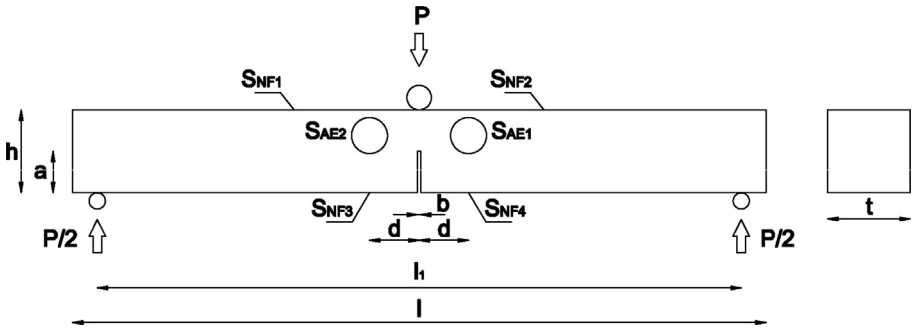

Fig. 1. Specimen geometry and loading configuration: S_{AE1} and S_{AE2} denote the broadband and resonant AE sensors, respectively; S_{NF1}–S_{NF4} denote the sensors used for the resonant frequency identification.

bending may show a more unstable crack growth than in three-point bending configuration [28]. This fact is also confirmed by the results of the tests performed by the authors. Furthermore, unlike the four-point bending case, for a specimen with a notch at mid-length tested under displacement-controlled three-point bending, the cracking section represents a nodal section for all mode shapes (the scheme is similar to that of a beam on three supports, the central one of which is subjected to an imposed displacement): this makes the DI particularly challenging. This case is also of practical interest since, although with the due differences, a similar situation may be encountered in real structures: for example, in continuous beams resting on three supports, like those of many two-span bridges, cracks may develop at the extrados in correspondence of the central support, where the maximum negative bending moment takes place.

As in [27], also here the AE and DI techniques are seen as complementary tools: the first revealing micro-cracks formation and macro-crack propagation in terms of AE frequency and emitted energy; the second giving information about the reduction in stiffness – and, therefore, in loading capacity – due to crack propagation in terms of resonant frequency decrease. Numerical finite element models, implemented in a commercial code, complete the study with the aim of correlating the measured bending frequencies to the crack advancement.

2. Experimental tests and results

2.1. Specimens, experimental set-up and procedures

Tests were conducted on two concrete beam samples having length $l = 84$ cm and square cross-section of side 10 cm. The samples were pre-notched at mid-length for half of the depth (notch width equal to 4 mm). The specimens geometry and the loading configuration are shown in Fig. 1, while the geometric dimensions are listed in Table 1. Specimens features and experimental set-up were defined according to RILEM TC 50-FMC protocol [29]. Values of mass density $\rho = 2310\,kg/m^3$ and compression strength $R_c = 26.4$ MPa were obtained averaging measures made on five concrete cubic specimens of side 16 cm.

The specimens were tested, up to final failure, on a servo-hydraulic MTS machine by controlling the vertical displacement of the hydraulic jack. The specimens were equipped with four JPR Plustone 400-403 piezoelectric pickups (outer diameter 20 mm, frequency range ~0–20 kHz, resonant frequency 6 ± 0.5 kHz, operating temperature −20 to +50 °C, weight ~1 g) for the extraction of resonant frequencies [30] and two piezoelectric AE detectors (by LeaneNet S.r.l., Sarzana, Italy), one of broadband (S_{AE1}) and one of resonant (S_{AE2}) type (frequency range of S_{AE1} = 80–400 kHz; resonant frequency of S_{AE2} = 160 kHz; cylindrical aluminum case dimensions: diameter 50 mm, thickness 35 mm; weight 110 g). Broadband sensors have wider operating frequency range and lower sensitivity than resonant sensors. The latter are to be preferred when monitoring elements of heterogeneous materials or large structures, as well as if accurate damage localization is required. In this study, despite AE data of both the two sensors applied were acquired, only those captured by the resonant sensor S_{AE2} were analyzed. The pickups were coupled to an 8-channel Audiobox 1818VS1 acquisition device (by PreSonus; Baton Rouge, LA, USA); the sampling frequency was set to 48 kHz. The AE sensors were connected to an 8-channel National Instruments digitizer; the acquisition threshold was set equal to 5 mV and the sampling frequency equal to 1 MHz. Fig. 2 shows the experimental set-up of the three-point bending tests conducted. As regards the number of sensors used, we must say that, in fact, 4 pickups are redundant for the extraction of resonant frequencies, for which one sensor is, in line of principle, sufficient. By contrast, a larger number of AE sensors is required for source localization [31,32]. However, AE signal localization was not an objective of the present work.

Two different testing procedures were followed: type (a), where the controlled displacement was increased continuously, with a

Table 1
Geometric dimensions of the specimen in Fig. 1 (in mm).

l	h	t	a	b	l_1	d
840	100	100	50	4	780	60

Fig. 2. Experimental set-up of the three-point bending tests conducted.

velocity of 1 μm/s, up to final failure of the specimen, and during which the load vs. displacement curve and AE signals were recorded; and type (b), where the imposed displacement was increased in several steps, at the end of which the specimen was excited by an impulsive force and the free response signal acquired by the pickups to extract the resonant frequencies; load vs. displacement and AE data were acquired, too.

2.2. Experimental results

Fig. 3 shows the load vs. displacement curves obtained from the two tests conducted: test 1 is of type (a), while test 2 is of type (b), as the discontinuous character of the relevant curve reflects. In particular, in test 2, the loading process was stopped ten times, for a total of eleven steps, the last one of which lead the specimen to fail; the load losses registered at the end of each step, and subsequent recovery, are due to the testing procedure adopted. The general trend of test 2 is, therefore, the one represented by the dashed line, obtained numerically by polynomial interpolation of the experimental data. The load values reported in Fig. 3 indicate the force read by the loading cell during the test (mid-point force); they do not include the self-weights of specimen, sensors, etc. The displacement values in the same figure represent the vertical displacement of the hydraulic jack (i.e., the input of the test), relative to its starting value.

Both curves in Fig. 3 show an elasto-softening behavior of the specimens, with a stable crack propagation. Conversely, specimens of the same type tested in displacement controlled four-point bending (see [27]) showed a tendency toward an unstable crack growth in the post-peak branch: the global behavior was unstable in two cases on three, with large load drops (snap-downs hiding a snap-back phenomenon); the only stable case was registered in a test conducted by following the procedure of test type (b) described above. It must be noticed that, in fact, the specimens carried nearly the same maximum bending moment in the two loading configurations: the peak load, P_{max}, reached in three-point bending was about one half the peak load reached in four-point bending; this is coherent with the fact that the maximum bending moment acting in a three-point bending scheme (i.e., $P\ l_1/4$) is twice the maximum bending moment acting in a $l_1/4 - l_1/2 - l_1/4$ four-point bending scheme (i.e., $P\ l_1/8$). Moreover, by elementary calculations of linear elasticity and linear elastic fracture mechanics, one could show that, for both the analyzed cases, the maximum loading capacity is governed by material failure in tension (maximum bending stresses equal to concrete tensile strength) rather than

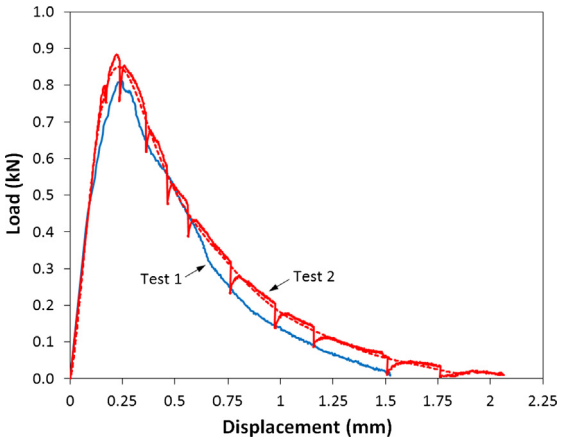

Fig. 3. Experimental load vs. displacement curves.

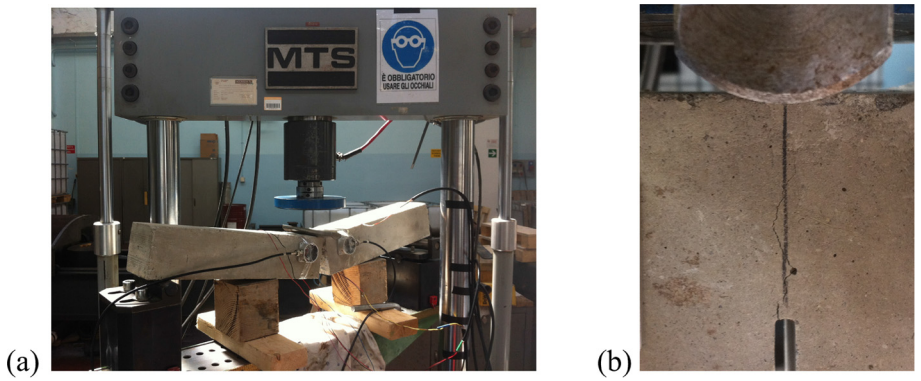

Fig. 4. (a) Failure mechanism and (b) crack path above the notch.

by reaching the fracture toughness (mode I stress intensity factor K_I equal to the critical value K_{IC}). At the same time, the ratio between the maximum vertical displacement and the displacement corresponding to the peak load P_{max} is much larger for the three-point bending tests than in the case of the four-point bending tests: these confirms the tendency of the latter case toward an unstable post-peak behavior.

Fig. 4a shows one of the two specimens tested in three-point bending at the end of the test. As it was expected, the failure occurred due to crack formation and propagation at mid-span, in correspondence to the notch (Fig. 4b): the crack path was sub-vertical, in agreement with a preeminent crack propagation in mode I. The other specimen showed the same behavior.

In Fig. 5a, b, the load vs. displacement and cumulative AE energy (from sensor S_{AE2}) vs. displacement diagrams of test 1, 2 are superimposed. The figure shows that, for both tests, no sensible AEs were detected until the peak load was reached, whereas a large jump in the AE energy was registered in correspondence to about half of the maximum vertical displacement.

Qualitative information on the classification of cracks can be obtained from AE signal parameters. Two indices are used to this purpose, namely average frequency (AF) and RA, which are defined, for each AE signal, from wave parameters as: Average frequency = Counts/Duration, RA = Rise time/Maximum amplitude. Counts are the number of amplitude threshold crossings; Duration is the time between first and last signal amplitude above the threshold level; Rise time is the time between the first threshold crossing and the time corresponding to the maximum signal amplitude. Tensile cracks (mode I) are characterized by relatively high AF and low RA values (P-waves). By contrast, shear cracks (mode II) are characterized by relatively low AF and high RA values (S-waves) [33–35]. Fig. 6a and b shows the average frequency vs. RA value diagrams for test 1 and 2, respectively (data from sensor S_{AE2}). Since most values lie to the left of the diagonal line, the damage progress is characterized by a dominant presence of tensile cracks.

In Fig. 7a, the variation of the first three vertical bending frequencies is superimposed to the load–displacement curve of test 2. It must be noted that ten values are reported for each frequency in correspondence to as many loading steps: each frequency value is the mean of twelve values, i.e., three reads for each one of the four sensors. As it is known, the natural frequencies decrease with damage, i.e., as the beam stiffness decreases with crack advancement: as it will be shown later on, this could be used to estimate the crack depth by means of numerical models, starting from measured frequency values [36]. The percentage variation of the frequencies with respect to their initial value is reported in the graph. Fig. 7b shows the mode shapes corresponding to the frequencies in Fig. 7a at the beginning of the test (i.e., for the initial notch depth), obtained by a 2-D finite element model implemented in LUSAS software [37] as

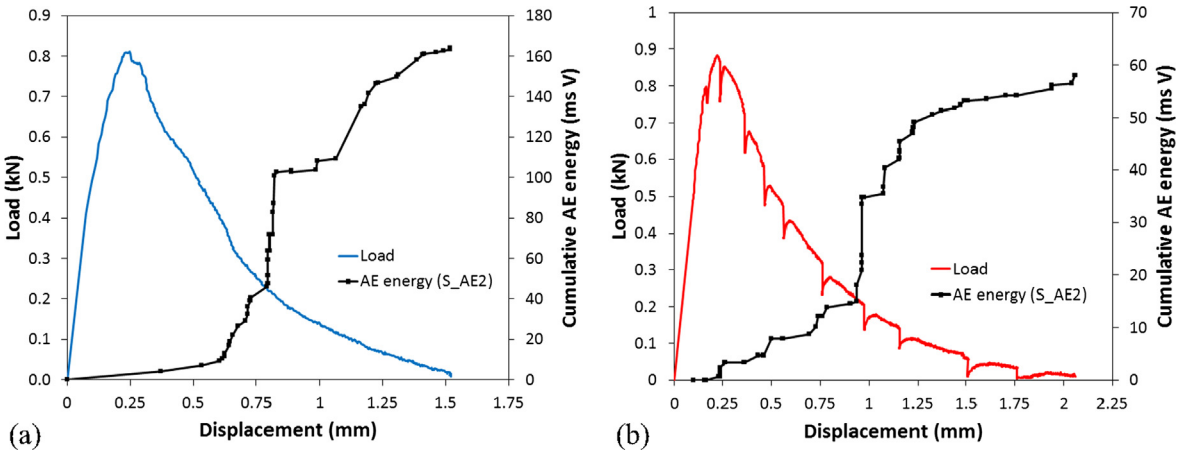

Fig. 5. Load and cumulative AE energy vs. displacement curves for (a) test 1 and (b) test 2.

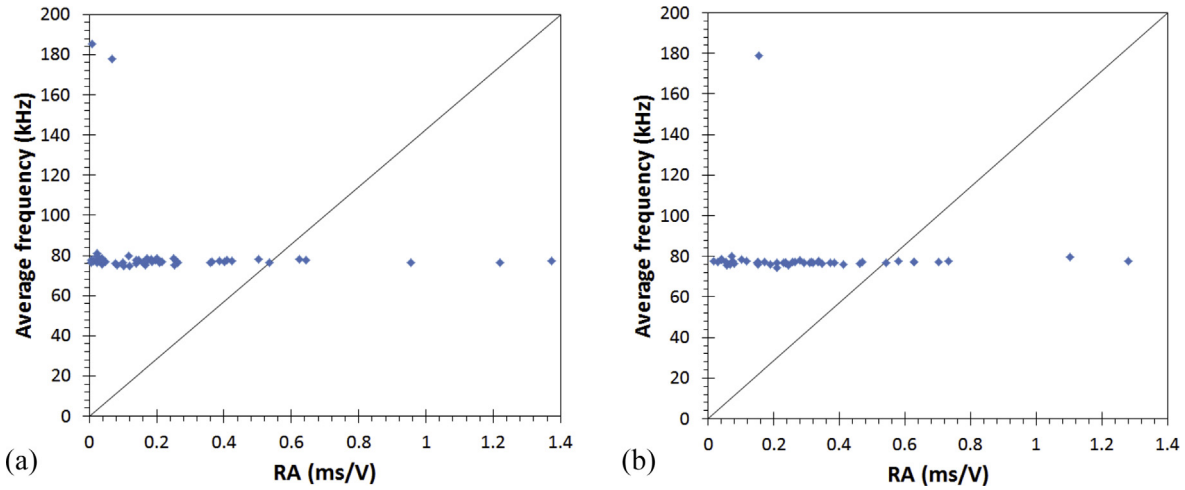

Fig. 6. Average frequency vs. RA values for (a) test 1 and (b) test 2 (from sensor S_{AE2}).

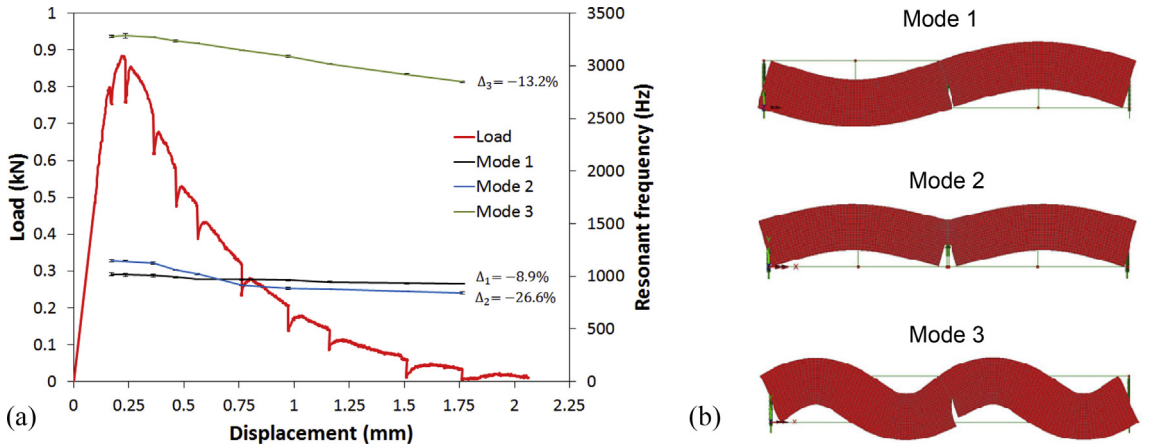

Fig. 7. (a) Experimental load and first three resonant frequencies vs. displacement curves for test 2; (b) first three initial mode shapes from finite element analysis.

described in Section 3: mode 1 is antisymmetric with a node at the center, mode 2 is symmetric with a node at the center, mode 3 is antisymmetric with three nodes; as pointed out before, all modes present a node in correspondence to the central support (notched section). It is interesting to note that, after a certain displacement (or crack depth), more precisely between steps 5 and 6, mode 2 prevails on mode 1 and becomes the fundamental mode (see the frequency crossing in Fig. 7a): the first antisymmetric mode prevails during the initial phase, while the first symmetric mode becomes predominant when the ligament is sensibly reduced. A numerical study on this point is presented in Section 3. The variation of each singular frequency with the imposed vertical displacement is shown in Fig. 8, where an indicator of the standard deviation is superimposed to each mean experimental value. The relatively small values of the standard deviation confirm that, as pointed-out before, even one or two pick-ups would have been sufficient.

3. Numerical simulations

Numerical finite element models of the beam were implemented in LUSAS by using plane stress elements. A first model was built using three-node triangular elements (TPM3) and adopting a nonlinear constitutive relation, both in tension and compression, for concrete. For the latter, the so-called Smoothed Multi Crack Model (Model 102) was used with the following mechanical parameters: uniaxial (cylindrical) compressive strength $f_c = 21.9$ MPa; uniaxial tensile strength $f_t = 2.4$ MPa; fracture energy $G_F = 184$ J/m^2. The values of f_c and f_t were evaluated, according to Eurocode 2 [38], starting from the measured value of R_c reported in Section 2.1; the value of G_F was evaluated experimentally according to RILEM TC 50-FMC protocol [29]. The triangular shape of the plane stress finite elements was selected to model the crack formation and propagation easily. A nonlinear static analysis was run on this model to obtain the load vs. deflection curve. The result is shown in Fig. 9, where the numerical curves are superimposed to the experimental ones: the dashed black line refers to the total acting load (mid-span force P plus the beam self weight), while the continuous black line refers to the mid-span force P only, as is for the experimental curves. As can easily be seen, the numerical curve reproduces pretty well

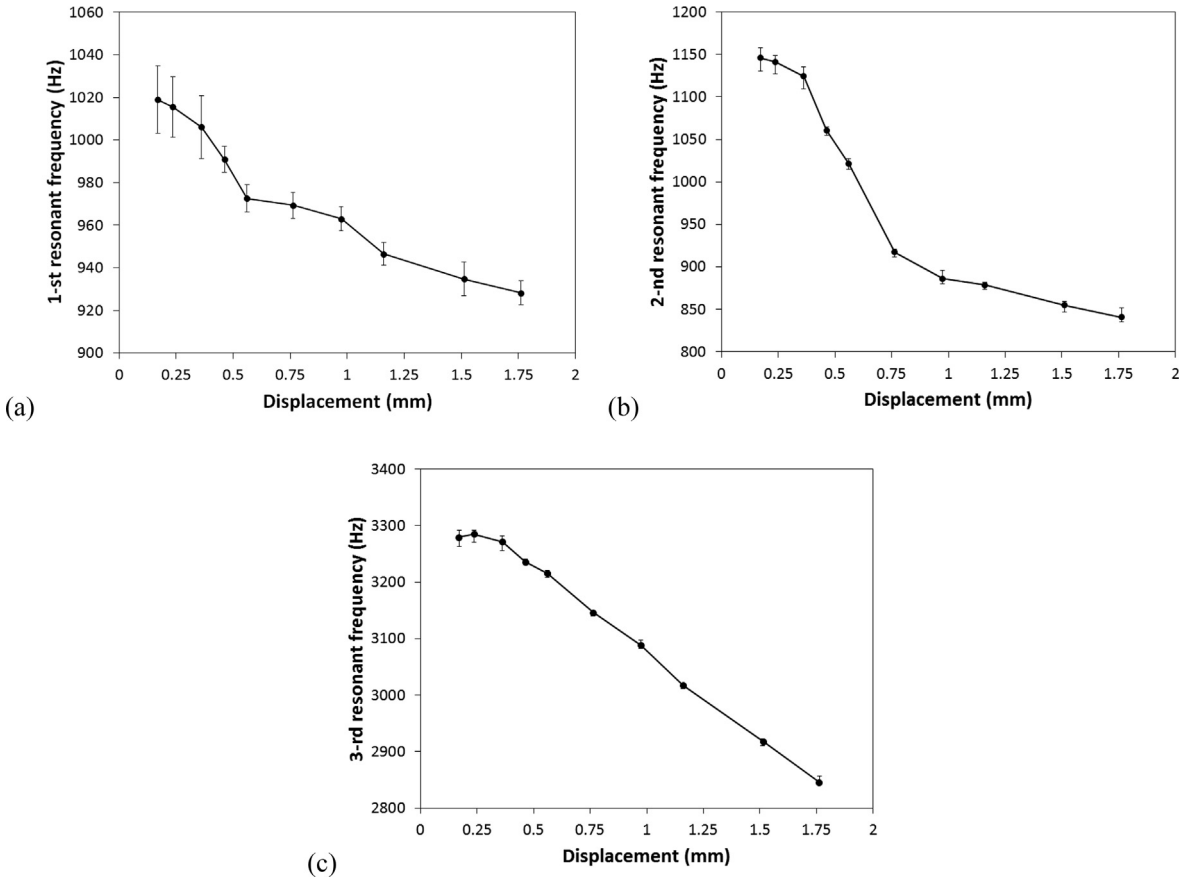

Fig. 8. (a) First, (b) second, and (c) third resonant frequency vs. displacement experimental curves for test 2.

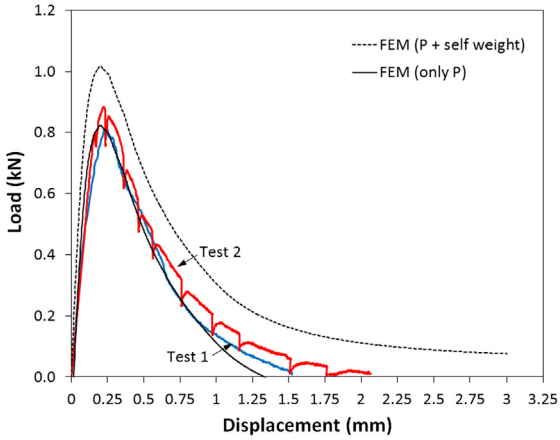

Fig. 9. Numerical (FEM) vs. experimental (tests 1 and 2) load–deflection curves.

the experimental trends.

A slightly modified model was built to calculate the natural vibration frequencies. In this case, the mesh was made using four-node quadrilateral elements (QPM4), while a linear elastic constitutive model was adopted for the material (Young's modulus E = 30,570 MPa; Poisson's ratio = 0.2; mass density $\rho = 2310\ \mathrm{kg/m^3}$ – see Section 2.1 and [38]). The beam was constrained by preventing the vertical displacements in correspondence to the end and intermediate sections. Free vibration analyses were run for increasing values of the relative notch depth a/h, from 0.5 (initial value) to 0.95, with a resolution of 0.05. In this case, the quadrilateral shape of the finite elements was selected for ease of modeling: the ligament was discretized in 10 equal parts (5 mm each) in vertical direction, such that each increment of 0.05 in a/h was simply obtained by removing a single part. The analyses were all run

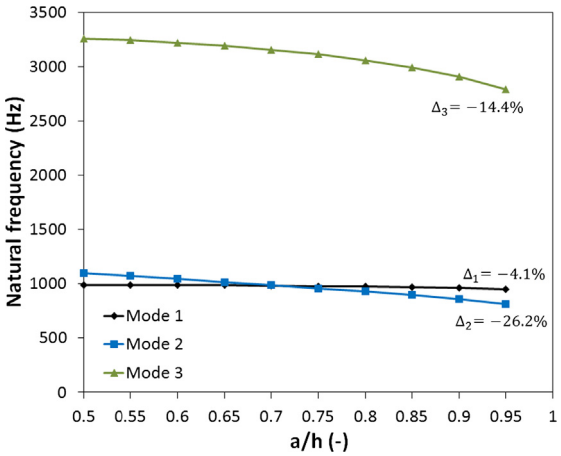

Fig. 10. Numerical (FEM) natural frequencies vs. relative notch depth a/h.

with respect to the undeformed configuration, in stress-free conditions, since geometric nonlinearity effects are negligible for the problem under consideration. In Fig. 10, the first three numerical natural frequency vs. relative notch depth curves are plotted; the percentage variations with respect to the initial values are also reported. The curves are all concave, showing a monotonic decrease of the frequencies, with a negative slope which becomes steeper as the ratio a/h is increased. We also note that the numerical results confirm the occurrence of the frequency (mode) crossing evidenced by the experimental curves (see Fig. 7a): according to the numerical prediction (Fig. 10), this happens for $a/h = 0.7$. Fig. 11 shows the sequences of the first three modes as given by the calculations for values of the ratio a/h equal to 0.75 and to 0.95 (compare to Fig. 7b). Actually, for $a/h > 0.7$ the symmetric mode (previously denoted as mode 2) becomes the fundamental one.

A comparison between Figs. 8 and 10 shows that there is a good match between the initial values of the measured and calculated frequencies. Most importantly, from Figs. 7a and 10 we see that the experimental and numerical trends show very similar percentage decreases for the frequencies of modes 2 (symmetric) and 3 (second antisymmetric), whereas it is not so for the one associated to mode 1 (first antisymmetric); for the latter, the numerical prediction is, therefore, not reliable. On the other hand, the first antisymmetric mode (denoted as mode 1) is the one which results less affected by a notch at mid-span, as can easily be seen from Fig. 7b and 11. In fact, the most interesting mode among all is surely the symmetric one (mode 2), which represents the fundamental vibration mode at the final stages of the damage process. Thus, its frequency can be used to make an estimate of the crack advancement. To this purpose, in Fig. 12 the experimental frequency values of mode 2 (red circles) are superimposed to the corresponding numerical values (blue line with square markers), plotted as a function of the relative notch depth. The red numbers close to the circles indicate the loading steps of test 2. In the figure, the frequency values have been nondimensionalized with respect to the relevant initial values in order to make the comparison in terms of purely percentage variation, the measured and calculated frequencies having shown practically the same final percentage decrease. According to the results in Fig. 12, for example, step 5 can be associated to $a/h = 0.71$, step 6 to $a/h = 0.87$, and so on. A similar procedure can conveniently be used to evaluate the damage severity in similar situations that can be encountered in practice.

In Fig. 12, we compared numerical natural (i.e., undamped) frequencies with the corresponding measured resonant frequencies, which are damped. It must be noticed that: (i) in practice, the values of damped and undamped frequency are very close each other; (ii) the frequency decrease induced by stiffness reduction due to damage (like cracking) is much larger than the frequency reduction

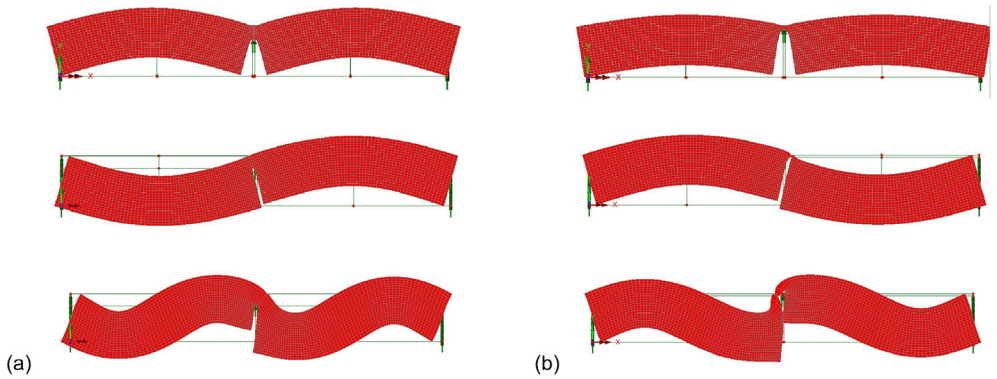

Fig. 11. First three numerical (FEM) mode shapes for relative notch depths a/h equal to (a) 0.75 and (b) 0.95: for $a/h > 0.7$ the symmetric mode becomes the fundamental one.

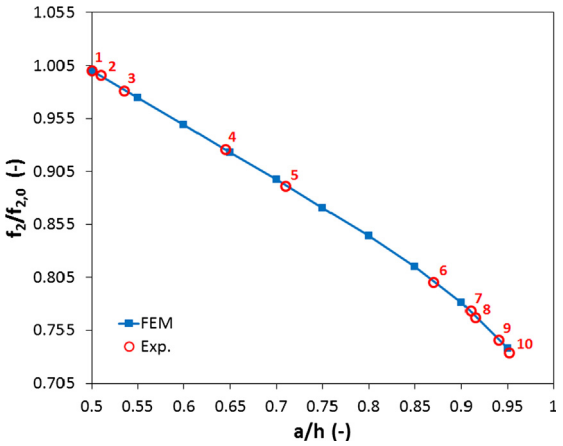

Fig. 12. Estimate of the crack advancement based on the superposition of measured frequencies on the calculated frequency vs. relative notch depth curve for the first symmetric vibration mode (numbers close to red circles indicate the loading steps of test 2). (For interpretation of the references to colour in this figure legend, the reader is referred to the web version of this article.)

induced by the increase of mechanical (internal) damping due to damage. At the same time, measuring damping parameters (e.g., damping ratio) can give information about damage progress: however, in practice, evaluating damping for multi-degree-of-freedom systems is sensibly more complicated than extracting resonant frequencies.

4. Conclusions

The study focused on the monitoring of the crack propagation process in a pre-notched concrete beam specimen, tested in displacement controlled three-point bending, by the Acoustic Emission (AE) technique and the extraction of resonant frequencies. The results showed how the cumulative AE energy can effectively be used to follow a damage progress due to crack propagation, although it gives no quantitative information about the damaging level as it is not an absolute parameter. On the other hand, useful information about the prevailing crack propagation mode – i.e., mode I (opening) or mode II (sliding) – can be obtained from average frequency (AF) vs. RA value analysis. At the same time, the decrease in the resonant frequencies gives direct information on the structural stiffness reduction due to crack propagation; this reduction in stiffness can be correlated to the damage severity by means of numerical models. To this purpose, a finite element model was built to evaluate the natural frequencies and modes for increasing notch depths: therefore, a comparison between measured and calculated frequencies allowed for a good estimate of the crack advancement. This seems to open the way to possible application in the monitoring of real concrete beams, where the use of simplified methods giving a realistic estimate the damage level is of great usefulness. In fact, too sophisticated models are often not needed in practice, especially when the level of detail of the theoretical result goes beyond the uncertainty upon the real parameters involved.

Acknowledgments

The authors gratefully acknowledge Eng. Davide Barone for his helpful contribution in the acquisition and analysis of experimental data.

References

[1] Acoustic emission and related non-destructive evaluation techniques in the fracture mechanics of concrete. Woodhead Publishing; 2015.
[2] Ohno K, Ohtsu M. Crack classification in concrete based on acoustic emission. Constr Build Mater 2010;24:2339–46.
[3] Aggelis DG. Classification of cracking mode in concrete by acoustic emission parameters. Mech Res Commun 2011;38:153–7.
[4] Aldahdooh MAA, Bunnori NM. Crack classification in reinforced concrete beams with varying thicknesses by mean of acoustic emission signal features. Constr Build Mater 2013;45:282–8.
[5] Carpinteri A, Lacidogna G, Pugno N. Structural damage diagnosis and life-time assessment by acoustic emission monitoring. Eng Fract Mech 2007;74:273–89.
[6] Carpinteri A, Lacidogna G, Puzzi S. From criticality to final collapse: evolution of the *b*-value from 1.5 to 1.0. Chaos Soliton Fract 2009;41:843–53.
[7] Xu J, Fu Z, Han Q, Lacidogna G, Carpinteri A. Micro-cracking monitoring and fracture evaluation for crumb rubber concrete based on acoustic emission techniques. Struct Health Monit 2017:1–13. https://doi.org/10.1177/1475921717730538.
[8] Ongpeng JMC, Oreta AWC, Hirose S. Monitoring damage using acoustic emission source location and computational geometry in reinforced concrete beams. Appl Sci 2018;8:189. https://doi.org/10.3390/app8020189.
[9] Carpinteri A, Corrado M, Lacidogna G. Heterogeneous materials in compression: correlations between absorbed, released and acoustic emission energies. Eng Fail Anal 2013;33:236–50.
[10] Carpinteri A, Lacidogna G, Corrado M, Di Battista E. Cracking and crackling in concrete-like materials: a dynamic energy balance. Eng Fract Mech 2016;155:130–44.
[11] Virgin LN. Vibration of axially loaded structures. New York: Cambridge University Press; 2007.
[12] Carpinteri A, Malvano R, Manuello A, Piana G. Fundamental frequency evolution in slender beams subjected to imposed axial displacements. J Sound Vib 2014;333:2390–403.
[13] Piana G, Lofrano E, Manuello A, Ruta G. Natural frequencies and buckling of compressed non-symmetric thin-walled beams. Thin Wall Struct 2017;111:189–96.

[14] Piana G, Lofrano E, Manuello A, Ruta G, Carpinteri A. Compressive buckling for symmetric TWB with non-zero warping stiffness. Eng Struct 2017;135:246–58.
[15] Hearn G, Testa RB. Modal analysis damage detection in structures. J Struct Eng 1991;117(10):3042–63.
[16] Rizos PF, Aspragathos N, Dimarogonas AD. Identification of crack location and magnitude in a cantilever beam from the vibration modes. J Sound Vib 1990;138(8):381–8.
[17] Doebling SW, Farrar CR, Prime MB, Shevitz DW. Damage identification and health monitoring of structural and mechanical systems from changes in their vibration characteristics: a literature review. Los Alamos Report LA-13070-MD, Los Alamos, USA; 1996.
[18] Hassiotis S, Jeong GD. Assessment of structural damage from natural frequency measurements. Comput Struct 1993;49(4):679–91.
[19] Pandey AK, Biswas M, Samman MM. Damage detection in structures using changes in flexibility. J Sound Vib 1994;169(1):3–17.
[20] Casas JR, Aparicio AC. Structural damage identification from dynamic-test data. J Struct Eng 1994;120(8):2437–50.
[21] Hassiotis S, Jeong GD. Identification of stiffness reduction using natural frequencies. J Eng Mech 1995;121(10):1106–13.
[22] Silva JMM, Gomes AJMA. Crack identification of simple structural elements through the use of natural frequency variations: the inverse problem. Proceedings of the IMAC XII conference, Honolulu, USA. 1994. p. 1728–35.
[23] Doyle JF. Determining the size and location of transverse cracks in beams. Exp Mech 1995;35(3):272–85.
[24] Khiem NT. Damage detection of beam by natural frequencies: general theory and procedure. Vietnam J Mech (VAST) 2006;28(2):120–32.
[25] Dessi D, Camerlengo G. Damage identification techniques via modal curvature analysis: overview and comparison. Mech Syst Signal Process 2015;52–53:181–205.
[26] Ewins DJ. Modal testing: theory, practice and application. 2nd ed. Baldock: Research Studies Press; 2000.
[27] Lacidogna G, Piana G, Carpinteri A. Acoustic emission and modal frequency variation in concrete specimens under four-point bending. Appl Sci 2017;7:339. https://doi.org/10.3390/app7040339.
[28] Tandon S, Faber KT, Bažant ZP. Crack stability in the fracture of cementitious materials. Mater Res Soc Symp Proc 1995;370:387–96.
[29] Draft Recommendation of RILEM TC 50-FMC. Determination of the fracture energy of mortar and concrete by means of three-point bend tests on notched beams. Mater Struct 1985;18:287–90.
[30] Piana G, Lofrano E, Carpinteri A, Paolone A, Ruta G. Experimental modal analysis of straight and curved slender beams by piezoelectric transducers. Meccanica 2016;51(11):2797–811.
[31] Carpinteri A, Xu J, Lacidogna G, Manuello A. Reliable onset time determination and source location of acoustic emissions in concrete structures. Cem Concr Compos 2012;34:529–37.
[32] Han Q, Xu J, Carpinteri A, Lacidogna G. Localization of acoustic emission sources in structural health monitoring of masonry bridge. Struct Control Health Monitor 2015;22:314–29.
[33] Recommendation of RILEM TC 212-ACD. Acoustic emission and related NDE techniques for crack detection and damage evaluation in concrete: measurement method for acoustic emission signals in concrete. Mater Struct 2010;43:1177–81.
[34] Recommendation of RILEM TC 212-ACD. Acoustic emission and related NDE techniques for crack detection and damage evaluation in concrete: test method for damage qualification of reinforced concrete beams by acoustic emission. Mater Struct 2010;43:1183–6.
[35] Recommendation of RILEM TC 212-ACD. Acoustic emission and related NDE techniques for crack detection and damage evaluation in concrete: test method for classification of active cracks in concrete by acoustic emission. Mater Struct 2010;43:1187–9.
[36] Jagdale PM, Chakrabarti MA. Free vibration analysis of cracked beam. Int J Eng Res Appl 2013;3(6):1172–6.
[37] LUSAS. User reference manual (version 15.1). Thames, Surrey, UK: FEA Ltd., Kingston upon; 2015.
[38] EN 1992-1-1:2004. Eurocode 2: Design of concrete structures – Part 1-1: general rules and rules for buildings.